Attosecond X-ray absorption fine-structure spectroscopy in condensed matter

by

Bárbara Buades

Thesis Advisor:
Prof. Dr. Jens Biegert

A thesis submitted in fulfillment of the requirements
for the degree of Doctor of Philosophy
in the

Attoscience and Ultrafast Optics

ICFO – Institut de Ciències Fotòniques
UPC – Universitat Politècnica de Catalunya

Barcelona, June 2018

3 Attosecond X-ray absorption fine-structure spectroscopy

In this chapter the capabilities of using the generated broadband attosecond pulses in the SXR regime are presented. Specifically, the simultaneous acquisition of the pulses' spectra offers the potential to explore the correlation between structural and electron dynamics via X-ray absorption fine structure spectroscopy (XAFS). In addition, using the XAFS technique with radiation that is confined in a pulse duration shorter than the core-hole decay of the elements brings a new insight into the electronic dynamic processes involved during the XAFS measurements.

An introduction of the XAFS technique is first given in Sec. 3.1. This technique is applied to a graphite flake at the carbon K-shell edge to demonstrate the capability of simultaneously probing the graphite's orbitals via near-edge XAFS (NEXFAS or XANES), shown in Sec. 3.2.1, and its structure via extended XAFS (EXAFS), presented in Sec. 3.2.2. Afterwards XAFS spectra using attosecond pulses are compared with XAFS spectra using picosecond pulses from synchrotron facilities. The comparison is performed on graphite and TiS_2, from which spectral resolved Auger electrons are also capture only using synchrotron radiation. The chapter finishes with the conclusions of the presented results in Sec. 3.4.

3.1 Introduction to attoXAFS

X-ray absorption fine-structure (XAFS) spectroscopy is a powerful element-specific technique, providing electronic, structural, and chemical information with atomic resolution[91–94]. Using XAFS, electronic information is extracted from the near-edge XAFS (XANES or NEXAFS), which arises from transitions from inner-shell orbitals to unoccupied electronic states near the Fermi energy level. Its measurement requires high-energy resolution to resolve spectral features that occur within only a few eV. Structural information is obtained from the extended XAFS (EXAFS), which extends over several hundred eV above the absorption edge, and it arises from the scattering of photo-emitted core-electrons on neighbouring atoms. While XANES and EXAFS are both well-established methods, and quick-scan or dispersive setups permit a relatively rapid acquisition of EXAFS[95,96], crucially lacking so far was the capacity to connect the information embedded in XANES and EXAFS on the atto- to few-femtosecond temporal scale. Performing XAFS spectroscopy measurements using broadband attosecond pulses (attoXAFS) allow simultaneous direct access to electronic and nuclear couplings. Moreover, the ultrafast probing capability is essential to explore the dephasing caused by lattice reordering on a few-tens-of-fs timescale[97]. AttoXAFS therefore provides unprecedented insight into the connection between a material's electronic excitation and lattice reordering, opening the possibility to thus study the time evolution and phase transitions of a physical system.

Until now, the limiting factor for an implementation of attoXAFS was the X-ray sources. For instance, synchrotrons provide very high brightness and excellent spectral stability, but the hundreds of femtosecond to picosecond duration of the X-ray pulses are too long even from slicing sources[98]. The long pulse duration and the associated narrow spectra requires scanning or concatenation of XANES with dispersive EXAFS, thus preventing the extraction of correlated information. X-ray free electron lasers (XFELs) easily provide few-femtosecond duration bursts of X-ray radiation at extreme brilliance, but since the X-ray bursts originate from noise, they suffer from irreproducibility of the pulse's deeply modulated spectra and temporal profile. This irreproducibility presents an additional problem for XAFS, since data extraction requires measurement of an identical reference spectrum. Thus, with the advent of HHG light sources[99,100] novel tools for XAFS have emerged which can provide the desired attosecond temporal resolution with shot-to-shot reproducibility and contain a broadband spectrum. However, it is only recently that isolated, i.e. also ultra-broadband, attosecond pulses in the SXR water-window with sufficient flux have become available[39–41,55], thus providing the desired ultrafast temporal resolution in combination with sufficient spectral coverage in a photon energy range that offers element specificity.

Here, a generated attosecond SXR pulse is produced with a spectrum which covers the entire water window[40] including a spectral region 50 eV below the carbon K-edge (284 eV) up to the oxygen K-edge (543 eV), thus including the K-edge of nitrogen (410 eV) as well as many L and M edges[101] that are relevant to biology and material science, see Fig. 3.1.

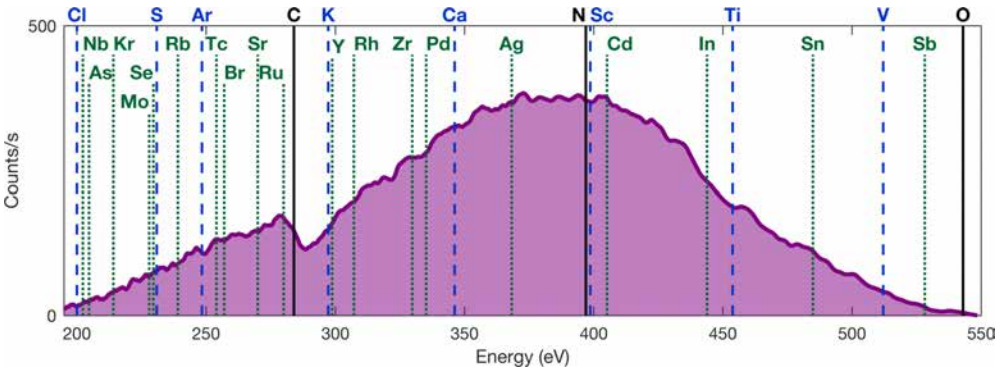

Fig. 3.1: Spectrum of the attosecond SXR pulse simultaneously covering the entire water window. The shown spectrum, taken from Fig. 1.6, is detected over an integration time of 1 minute with shuffled CEP. Overlaid with vertical lines which indicate the positions of accessible K-shell (black solid line), L-shell (blue dashed line) and M-shell (green dotted line) absorption edges. Elements with multiple absorption edges in this spectral region are indicated at the position where they present the strongest absorption edge.

3.1.1 XANES fundamentals

XAFS is based on the light-mater interaction through the photo-electric effect upon an inner core shell electron. An X-ray photon is absorbed by an electron in a tightly bound quantum core level of an atom. For the X-ray to be absorbed its photon energy, E, must be equal or greater than the binding energy of the electron, E_0 where $E \geq E_0$, yielding to the ejection of the electron with an energy, E_e, equal to the difference between the photon energy and the electronic binding energy, E_e = E - E_0. The ejected photo-electron with wave number k propagates away from the atom towards an available state described by the relation:

$$k = \frac{1}{\hbar}\sqrt{2m_e(E - E_0)}, \tag{3.1}$$

where m_e is the electron mass and $\hbar$ the reduced Planck constant. When the photon energy equals the electron binding energy, $E = E_0$, the absorption experiences a sharp rise so called absorption edge where the energy corresponds to the promotion of this core level electron to a minimum energetic available state. The inspection of spectral features close to the absorption edge is analogous to

revealing unoccupied density of states with angular momentum sensitivity above the Fermi level, and gives the name of the near edge XAFS (NEXAFS or XANES) spectroscopic technique. Since each element has different electron binding energies depending on the atomic number, the absorption edge is spectrally placed at particular energies. Hence, an X-ray photon energy range can be chosen to select specific absorption edges. Moreover, the available states where the core level electron is promoted to can only belong to the element from which the electron has been excited, giving XAFS spectroscopy an element-specific property.

The absorption of the radiation is given by the Beer's Law equation:

$$I = I_0 e^{-\mu t}, \tag{3.2}$$

where I and I_0 are the spectral intensities incident on a sample and transmitted through the sample, respectively, μ is the absorption coefficient and t is the sample thickness[102]. The absorption coefficient μ for energies above the absorption edge, depends on the sample density ρ, the atomic number Z, atomic mass A, and the X-ray energy E roughly as:

$$\mu \approx \frac{\rho Z^4}{AE^3}. \tag{3.3}$$

The XAFS spectral signal is experimentally recorded as μ(E) = - log(I/I_0). μ(E) is defined by the probability of a transition between two quantum states with the exact energy due to the presence of an external electric field given by Fermi's Golden Rule:

$$\mu(E) \propto \Gamma_{i\to f} = \frac{2\pi}{\hbar} \left|\langle f|H'|i\rangle\right|^2 \rho, \tag{3.4}$$

from the state $|i\rangle$ to a set of final states $|f\rangle$, where ρ is the density of final states and H' is the perturbation between the final and initial states. H' is the electron transition dipole operator given as H'= -e·$\tilde{d}\cdot\tilde{E}$ where e is the electric charge, $\tilde{d}$ is the dipole moment and $\tilde{E}$ is the electric field of the electromagnetic radiation[103]. H' in general, leads to the application of the dipole transition selection rule $\Delta l = \pm 1$, where l is the orbital (or angular) quantum number. The primary dipole transitions are from s to p, i.e. from a K shell (1s), or from p to d to, i.e. from a $L_{2,3}$ ($2p_{1/2,3/2}$). Hence, XAFS has orbital sensitivity because the core level electron excitation depends on the orbital character of the empty final states. The $\tilde{d}\cdot\tilde{E}$ dependency provides information about the anisotropy of the material and chemical composition giving a unique finger print for each sample under study.

XAFS spectroscopy places a few constrains on the sample under study. The sample is required to have high enough density to efficiently absorb the SXR radiation, while still transmitting a detectable signal above the absorption edge. The optimum XAFS signal is achieved at a normalised absorption jump = 1. This is

not possible in samples which are composed by more than one element. In that case the sample thickness has to be adjusted such that the jump is maximised. In this study, the sample thickness of the materials are chosen by maximising their absorptions jumps using the spectral transmission data given by the Ref. Thomson et al., 2001[101]. As SXR radiation is measured in transmission the spectra are largely insensitive to surface properties. For XAFS measurements the samples are prepared under atmospheric conditions and then transferred into the vacuum experimental chamber with no need of extra sample preparation.

3.1.2 EXAFS fundamentals

In a XAFS measurement, the ejected photo-electron from the photo-electric effect can be scattered by the neighbouring atom, and return to the initial absorbing atom. The electrons with a wavenumber k, Eq.(3.1), can interfere constructively or destructively yielding a change in the electronic density that is probed leading to oscillations on the spectrum above the absorption edge, is the so called EXAFS region. The photo-electron wave-function is considered to travel as a spherical wave with a damping spherical component (where λ_e is the mean-free-path of the photo-electron) to account for both the inelastic scattering and the core-hole lifetime. The photo-electron needs to travel a distance R between atoms, inelastically scatter and return to the absorbing atom before the core-hole is filled. This effect limits the maximum distance that the electron can travel before being detected to neighbouring atoms of around 5 angstroms.

The probability of the absorption being modulated is given as[104]:

$$\chi(k) = S_0^2 \sum_j N_j f_j(R_j, k) \frac{e^{-2\sigma_j^2 k^2} e^{-\frac{2R_j}{\lambda_{ej}(k)}}}{kR_j^2} sin\left(2kR_j + \delta_j(k)\right), \qquad (3.5)$$

where the amplitude of this equation is proportional to the amplitude of the scattered photo-electron at the absorbing atom S_0 and the sum of the contributions from each scattering atom type j. $f_j(R_j, k)$ and $\delta_j(k)$ are scattering properties of the neighbouring atom which depend on Z, these being the scattering factor and the phase shift, respectively, which are related to the potential of the absorbing atom. N is the coordination number and σ^2 is the mean-square-displacement in the bond distance R. The Debye-Waller term, $e^{-2\sigma_j^2 k^2}$, accounts for damping due to static and thermal disorder in absorber-backscattered distances.

The EXAFS oscillations consists of different frequencies that correspond to the different distances for each coordination shell, which leads us to use Fourier transforms in the analysis. Finally, in order to extract the distances and coordina-

tion numbers, softwares such as Athena and Artemis can be used to process and analyse the data from which the values for the scattering amplitude and phase-shifts $f_j(R_j, k)$ and $\delta_j(k)$ are extracted accurately.

3.1.3 XAFS core-hole decay

After photo-electron excitation during the absorption process in XAFS the atomic system is left in a highly untestable excited state that will decay within a few femtoseconds. There are two main decay channels, X-ray fluorescence and Auger effect[105–107]. The fluorescence consists of a decay of an electron from a higher energy shell to the hole originated in an inner-core shell by emitting a photon with a well defined energy. The Auger effect consists of an electron dropping from a higher electron level and a second electron being emitted into the continuum. In the soft X-ray regime for light atoms with $Z < 30$, the Auger effect is dominant[105].

XAFS spectroscopy using pulses with durations longer than a few femtoseconds are used to examine electronic states that are modified already by the long probing X-ray pulses. Previous XAFS measurements using radiation longer than tens of femtoseconds have not considered fluorescence and Auger decays to effects the XAFS signal. Nonetheless, disagreements between theoretical XAFS descriptions and experiments were related to Auger effects by assigning spectral broadenings to a decrease in life-time due to Coster-Kronig Auger decay[108]. It was not until recently that Auger electron spectroscopy (AES) was used to study electron dynamics involved in the relaxation processes after the absorption of X-rays[109,110].

The detection of electrons emitted from a sample is very sensitive to the surface composition since the electrons penetration depth is around a few nanometers[111–113]. This puts constraints upon the sample preparation. Sputtering or annealing of the sample needs to be performed under vacuum conditions just before the measurements in order to get rid of possible contaminants on the sample surface.

3.2 attoXAFS in graphite

In this section, the concept of attoXAFS in graphite is demonstrated with an isolated attosecond water-window SXR pulse that enables the simultaneous acquisition of carbon K-edge XANES and EXAFS, thus providing combined electronic and structural information. The spectrum contained in a sub-300-as-duration pulse[40] covers a region from 50 eV below the carbon K-edge (284 eV) up to more than

200 eV above it. A cutoff energy above 500 eV is obtained using the full energy of the 1.85 μm driving laser pulse for the HHG process as shown in Fig. 1.2. A maximised SXR flux is accomplished using a single metallic filter of aluminium with a thickness of 100 nm to block the left-over part of the driving laser radiation from the HHG process and transmit the whole water window spectrum.

Graphite consists of equally-oriented graphene layers, which interact via Van-der-Waals forces. In each graphene layer, the carbon atoms form strong covalent bonds and are orientated in a hexagonal lattice with four carbon atoms per unit cell[114–117]. Figure 3.2 shows a graphene layer in real space together with a layout of the energy levels in the reciprocal space displaying the different energy ranges probed by XANES and EXAFS at available states close to the Fermi energy level and to the continuum, respectively.

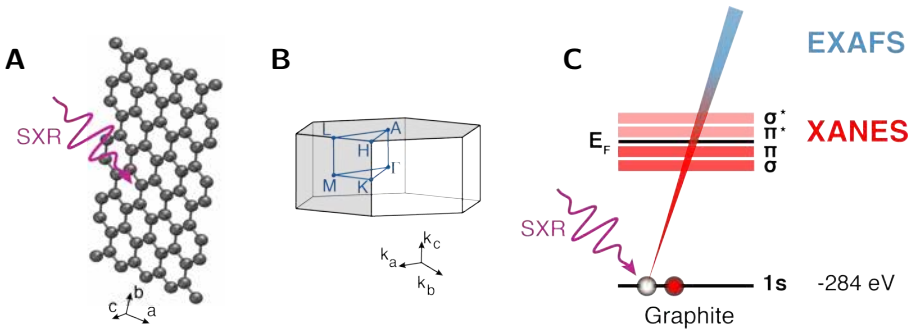

Fig. 3.2: Simultaneous XANES and EXAFS spectroscopy on Graphite. (**A**) Mono-layer honeycomb graphite structure (graphene). The first neighbour atomic distance is 0.142 nm[118]. The SXR wavelength between 2 and 4 nm has an averaged cycle period around 10 as. (**B**) Brillouin zone of the hexagonal lattice of graphite showing the main points and directions from where the band structure is calculated. (**C**) Shown are the sketches of the energy levels of graphite. The SXR radiation photoionises an inner core-shell electron 1s promoted to the σ^* and π^* p-like states in the conduction to perform simultaneous XANES and EXAFS.

Each carbon atom has six electrons of which two are located in the 1s core shell and the other four electrons occupy the valence shells ($2s^2$, $2p^2$). Three valence shell electrons form covalent bonds in graphite through a sp^2 hybridization. The fourth valence electron, has p symmetry with an orientation perpendicular to the graphene plane (p_z hereafter) and binds via Van-der-Waals forces to the neighbouring layers. The sp^2 orbitals form σ states in the sheet plane, and p_z forms a π state, which is the highest occupied state[117,119]. The antibonding states σ^* and π^*, are unoccupied in graphite and form the conduction band. The different symmetries of the two antibonding states, σ^* and π^*, become apparent when comparing the density of states (DOS) of the two different bands. Irradiating graphite with photons from around 200 eV to 500 eV causes the transition of the 1s

core-level electrons to both available p-like states in the conduction band for both the σ^* and π^* states, resulting in the XANES signal, this radiation also causes the electron to be emitted to the continuum resulting in the EXAFS signal, although there is not exist a hard boundary between XANES and EXAFS.

A graphite flake with a homogeneous thickness of 95 nm across an area with a diameter larger than of 50 μm can be manufactured using a dry-transfer technique[120]. Firstly, graphite flakes are exfoliated and deposited on a transparent polymer (Gel-Pak gelfilms). Suitable flakes are identified under the optical microscope and deterministically transferred onto a 50 nm thick Si_3N_4 membrane using a x-y-z micromanipulator stage. The advantage of this transfer method is that the graphite flakes are never in contact with any wet solvents, therefore minimizing their contamination while maintaining an atomically flat surface. After the transfer, the thickness of the graphite flake is characterised using atomic force microscopy (AFM). Finally, a pinhole with a diameter of 50 μm is placed on a selected area of the flake, where it is homogeneous, again using the micromanipulator stage. The sample assembly is shown in Fig. 3.3. Homogeneity on the sample ensures that the SXR radiations travels through the whole same thickness. Crystallization provides a uniform anisotropy across the entire sample.

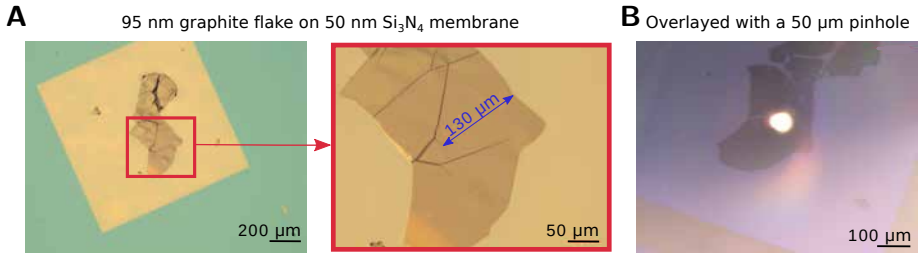

Fig. 3.3: 95 nm graphite sample assembly. (**A**) A 95 nm graphite flake sitting on a 1 mm x 1 mm x 50 nm Si_3N_4 membrane. Zoomed in, shown on the right, there is the found homogeneous area with a width over 130 μm that is used as sample. (**B**) Illuminated in transmission can be seen the light going through the pinhole which overlaps the homogeneous area found in the graphite flake. The images are taken with a microscope (Axio Scope; Carl Zeiss) using 5x, 20x and 10x magnification, respectively.

The attoXAFS signal simultaneously measuring the XANES and EXAFS spectral ranges is taken by measuring the transmitted SXR radiation through the 95 nm graphite flake placed on the membrane, I, and through only the membrane as a reference signal, I_0, using the relation -log(I/I_0). The three signals, I, I_0 and attoXAFS signal, are shown in Fig. 3.4. The attoXAFS signal is normalised to a jump of 1 from below the absorption edge at energies well above ($>$ 50 eV) the absorption edge.

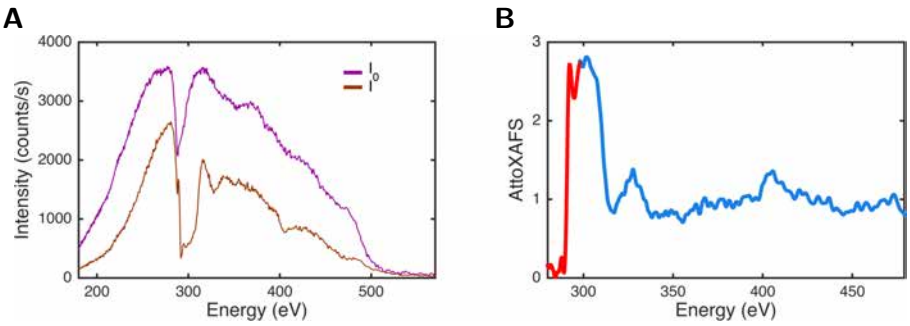

Fig. 3.4: Simultaneous XANES and EXAFS spectroscopy on Graphite. (**A**) Detected SXR spectral photon counts/s of the reference signal, I_0, measured after propagating through a 50 nm Si_3N_4 membrane; and of the transmitted signal, I, through a 95 nm graphite flake resting on a 50 nm Si_3N_4 membrane. Both spectra are the average over 6 spectra taken with 10 second integration times. (**B**) AttoXAFS signal which shows XANES features at 284 eV and EXAFS oscillations up to 200 eV above the absorption edge. The XANES range is highlighted in red and the EXAFS in blue. Note that no hard boundary exists between XANES and EXAFS and that the colour separation is solely chosen to indicate the predominant contribution to the measurement.

3.2.1 Orbital probing - XANES

XANES at the carbon K-shell edge results from dipole-allowed transitions from the 1s state to the lowest unoccupied states, σ^* and π^* and a part to the continuum. The σ^* and π^* states have a different symmetry, the σ^* state is confined in the basal plane of the graphite sample and the π^* state is perpendicular to it. Figure 3.5 show the corresponding minimum energetic available states at the conduction band calculated with the density functional theory (DFT) code BAND[121–123] using a local density approximation (LDA) exchange correlation functional with Triple zeta plus double polarization basis set[124]. The linear polarisation of the attosecond SXR radiation allows σ^* and π^* states to be distinguished by projecting the electric field $\tilde{E}$ onto the distinct dipole moment $\tilde{d}$'s directions. This is achieved when changing the angle of incidence of the SXR beam in a p-polarisation (polarisation parallel to the plane of incidence) configuration.

Figure 3.6 shows the XANES part of the normalized attoXAFS spectrum taken at different incident angles of the linearly-polarized attosecond SXR pulses with respect to the graphite basal plane normal. Independent of the incident angle, there is a clear rising edge at (292.6 $\pm$ 0.3) eV, which is followed by undulations of the absorption spectrum. From symmetry considerations, it is apparent that the edge arises due to the transition from the 1s core level to the minimum energetic available states indicated in Fig. 3.5.

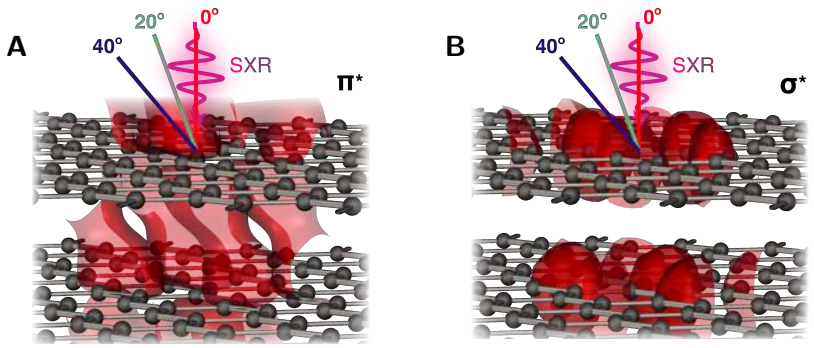

Fig. 3.5: DOS of the lowest unoccupied states π^* and σ^* in the conduction band. (**A**) π^* state, DOS perpendicular to the basal plane in the k-space direction from Γ point $\rightarrow$ A point. (**B**) σ^* state, DOS in the basal plane in the k-space direction from Γ point $\rightarrow$ M point.

Varying the incidence angle from 0 deg. to 20 deg., a second peak appears at (285.5 $\pm$ 0.3) eV with an amplitude that increases as the incident angle is further increased to 35 deg. The clear field polarization dependence of the peak at 285.5 eV allows us to identify this as a transition since the π^* is formed by p_z that is orientated perpendicular to the sample plane. At normal incidence, graphite's basal plane is perpendicular to the beam propagation direction, thus the attosecond pulse's linearly-polarized electric field probed only in-plane states, σ^*, consisting of sp^2. By tilting the sample, hence changing the angle of incidence from 0 deg. to 35 deg., an electric field component along p_z is induced, which excites the transition. These features, measured with the attosecond source, are in excellent agreement with predicted values as well as with electronic transitions[125–132] measured at synchrotron light sources. It is worth mentioning that the identified features are different from optical absorption measurements in which the transition is only excited for in-plane polarization[117], thus the difference with an X-ray measurement arises from the different initial states leading to different symmetry-allowed final states. The attoXAFS measurement accuracy is also sufficient to identify the weak feature, between the π^* and σ^* resonances at about 289 eV, this interlayer state arises from small residual material impurities[132].

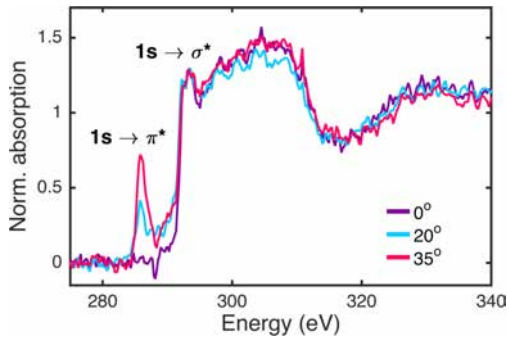

Fig. 3.6: Angle dependence XANES region of the attoXAFS spectrum. The incident attosecond SXR pulse is varied with respect to the basal plane normal of the sample. Normal incidence (0 deg.) probes states in the basal plane whilst any deviation from normal incidence also probes components out of the basal plane. Two main features can be identified at 285.5 eV and 292.5 eV, corresponding to 1s $\rightarrow \pi^*$ and $\rightarrow \sigma^*$ transitions, respectively.

3.2.2 Structural probing - EXAFS

The EXAFS region is analysed to retrieve information about graphite's lattice conformation. The oscillating spectrum above the absorption edge comes from the interference of excited photoelectrons with backscattered photoelectrons originating from neighbouring lattice atoms leading to constructive and destructive interference of the absorbing atom's electronic density. Figure 3.7 shows a sketch of the photo-electron interferences in a graphite layer sample over-layered with the identified bond distances.

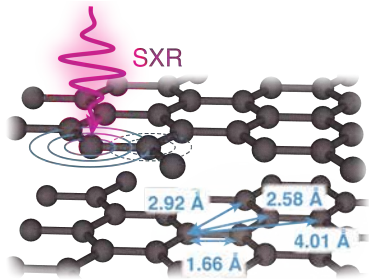

Fig. 3.7: EXAFS photo-electron interferences with extracted bond-distances. Two layers of graphite together with the identified bond distances after analysing a EXAFS spectrum from attoXAFS.

The blue part of the measured absorption curve, shown previously in Fig. 3.4, is now averaged over 7 spectra through the graphite sample, I, and 19 reference spectra, I_0. Each spectrum is taken with an integration time of 10 seconds at normal incidence. To deduce the bond length from these oscillations an analysis is

done with the Athena and Artemis software packages[133] and multiple scattering path simulations are performed with FEFF[134]. Firstly, the data in energy space are pre-edge corrected, normalized, deglitched (if necessary), and background corrected. The processed data is next converted to the photoelectron wave vector (k) space using Eq.(3.1), where E_0 is the origin energy or the threshold energy. The k-space data is truncated near the zero crossings ($k = 1.18$ Å^{-1} to 6.9 Å^{-1}) in EXAFS before Fourier transformation. The k-space data is transferred into the Artemis Software for curve fitting. Later, the EXAFS equation, Eq.(3.5), is used to fit the experimental Fourier transformed data (in R-space) as well as unfiltered data (in k-space) using N, S_0^2, E_0, R, and σ^2 as variable parameters. In order to fit the data, the Fourier peaks are either isolated separately, grouped together, or the entire (unfiltered) spectrum is used. The individual Fourier peaks are isolated by applying a Hanning window to the first and last 15% of the chosen range, leaving the middle 70% untouched. Afterwards, the curve fitting is performed using *ab initio-calculated* phases and amplitudes from the FEFF8[134,135] program and *ab initio-calculated* phases and amplitudes are used in the EXAFS equation, Eq.(3.5). The quality of the fit is evaluated by R-factor and the reduced χ^2 value. The deviation in E_0 is required to be less than or equal to 10 eV. An R-factor less than 2% denotes that the fit is good enough whereas an R-factor between 2% and 5% denotes that the fit is correct within a consistently broad model[104]. The reduced χ^2 value is used to compare the quality of the fit as more absorber-backscatter shells are included to fit the data. A smaller reduced χ^2 value indicates a better fit. Similar results are obtained from fits done in k, q, and R-spaces.

The reduced χ^2_{nu} is calculated by:

$$\chi^2_\nu = \frac{N_{ind}}{\nu N} \sum_{i=1}^{N} \frac{(data_i(x) - fit_i(x))^2}{\epsilon^2}, \tag{3.6}$$

where $data_i(x)$ and $fit_i(x)$ are the Fourier amplitude of the measured data and the fitted data, respectively. N_{ind} is the number of independent points, N is the number of data points, ϵ is the measurement uncertainties (noise level in the data) and ν is the number of degrees of freedom of the fit. The R-factor is another way to measure the fit quality and gives information about a fractional misfit which is calculated by

$$\text{R-factor} = \frac{\sum_{i=1}^{N} (data_i(x) - fit_i(x))^2}{\sum_{i=1}^{N} (data_i(x))^2}. \tag{3.7}$$

Table 3.1 shows the chosen variable parameters to minimise χ^2 for two different fits. One with the inclusion of the second and third neighbour atoms and a second one with all neighbouring shells taken individually. The amplitude reduction factor, S_0^2 is fixed to 1 and the fit is carried out between 0.75 Å and 4 Å. The

second fit with taking individually each neighbour shell improves the EXAFS fit since it has a smaller χ^2 parameter.

Fit	Shell, N	R (Å) (error bars to 100th of Å)	E_0	σ^2	R-factor	Reduced χ^2
1	C-C_1, 3 C-$C_{2,3}$, 9 C-C_4, 6	1.64 (3) 2.95 (5) 4.04 (7)	1.47	0.0161 0.0109 0.0144	0.024	315
2	C-C_1, 3 C-C_2, 6 C-C_3, 3 C-C_4, 6	1.66 (4) 2.58 (12) 2.92 (3) 4.01 (10)	2.97	0.0219 0.0353 0.0289 0.0118	0.009	195

Table 3.1: EXAFS fit parameters. Parameters for the Eq.(3.5).

Figure 3.8 shows the data after background correction and conversion into wavenumber space together with the back transformed fit and the fit's uncertainty. Also shown is the Fourier transform with the curve fitting that is performed based on the EXAFS equation, Eq.(3.5), with scattering phases and amplitudes from FEFF8[134,135]. The transformed amplitudes in which three prominent peaks are identified correspond to the scattering contributions from the 1st, 2nd, 3rd and 4th neighbouring carbon atoms.

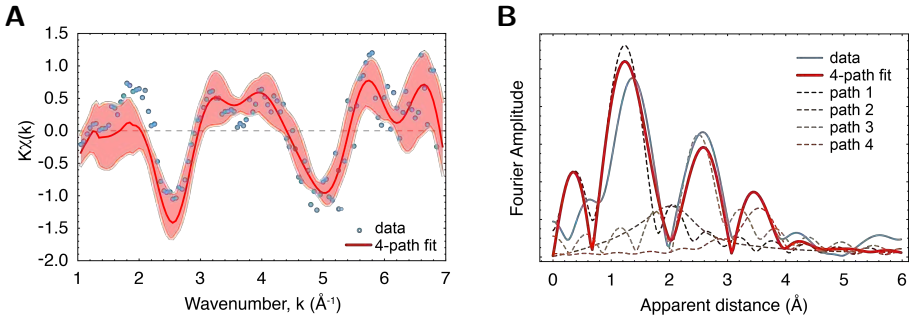

Fig. 3.8: EXAFS analysis. (**A**) The experimental EXAFS (blue circles) is shown together with the back transformed fit (solid red line) and the fit's uncertainty (red shaded area). (**B**) shows the Fourier amplitude of the experimental data together with the individual contributions from the first 4 scattering paths (dashed lines). The summed scattering contribution (solid red line), considering the scattering phases, results in a 2% fit accuracy. Note that the experimental spectra correspond to k values of 1.18 $Å^{-1}$ to 6.90 $Å^{-1}$.

Note that while only the amplitudes of the Fourier transform to R space are shown in Fig. 3.8, the fit takes the phase shifts also into account, thereby resulting in a fitting accuracy greater than 2%. From the fit the first apparent peak at

1.32 Å is identified which (in accordance with literature[136,137]) arises due to the scattering with the nearest neighbour at around 1.42 Å - 1.44 Å. The second peak represents the summed contribution of the second and third neighbour atoms at 2.47 Å and 2.87 Å with coordination numbers 6 and 3, respectively. Lastly, the third peak represents the scattering from the forth nearest carbon atom at around 3.77 Å.

To sum up the data analysis, from the absorption measurement in graphite we obtain the apparent distance of the neighbouring atoms directly from the Fourier transform of the EXAFS region. This data needs to be processed with the Artemis software that calculates the XAFS spectrum of graphite based on Eq.(3.5). We obtain from this the modelled bond distances in graphite that lead to the measured apparent distances.

Finally, the analysis of the overall spectrum yields bond distances of (1.66 $\pm$ 0.03) Å, (2.58 $\pm$ 0.12) Å, (2.92 $\pm$ 0.03) Å and (4.01 $\pm$ 0.10) Å. These bond distances from attoXAFS are found to be in excellent agreement with DFT calculations and carbon K-edge EXAFS measurements conducted at synchrotron sources[137].

3.3 XAFS core-hole decay - synchrotron vs. attosecond radiation

The highly unstable state left after the photo-induced excitation due to XAFS leads to a rapid relaxation of the system involving different electron dynamics. The goal is to investigate the possible ultrafast electronic reconfiguration upon X-ray pulse irradiation by comparing XAFS measurements on the attosecond with the picosecond domain. The interaction of the material with the picosecond X-ray pulse puts the material into a mixed and dressed state. We believe these electronic modifications could be caused by the following X-ray interactions:

1. **Electronic and vibrational dynamics**. Irradiation of a material with an X-ray pulse initiates core shell excitation thus forming a localised core-hole exciton which, in turn, modifies the valence potential. The high instability of the inner core shell vacancy will lead to an electronic relaxation within femtoseconds and consequently the emission of Auger electrons and/or high energy photons. Light atoms, with atomic number lower than 30, such as carbon, titanium, sulfur and silicon, have more than 90% probability of relaxing via an Auger decay channel regardless of photoemission[105] within a few femtoseconds. Both the inner core shell excitation and consecutive relaxation can trigger electronic dynamics on the femtosecond time scale,

thus initiating also vibrational dynamics. I.e. vibrational dynamics are most likely present during an XAFS measurement due to the long X-ray pulse duration. Unfortunately, the inclusion of such dynamics in condensed matter, both electronically and structural, is beyond current theoretical capabilities.

2. **Field effects on the energy levels**. X-ray absorption in an atom can occur at any time during the X-ray pulse duration with the same probability. But, the temporal variation of electric field amplitude along the X-ray pulse influences X-ray absorption differently. Thus, due to the low longitudinally coherence of synchrotron radiation, the X-ray interaction is best described with a non-oscillating dc electric field effect which predominantly disturbs energy levels of the outer electronic shells, i.e. valence states. Such external static field will induce a polarisation with a zero permanent dipole moment. The static electric field corresponding to a focused intensity of 0.3 GW/cm^2 (1 mJ, 10 ns, spot size of 100 μm) leads to a charge dislocation of approximately 10^{-4} Å. Note that the corresponding field strength is several orders of magnitude smaller than a molecular binding field. Both, synchrotron radiation and attosecond SXR radiation correspond to even lower field strengths, hence the quoted values indicated upper boundaries. For example, the flux of the SXR TEMPO beamline in SOLEIL synchrotron is 4x10^{13} photons/s/0.1%BW at a 352 MHz repetition rate focused to 30 μm x 80 μm area with a pulse duration of 30 ps. This leads to a focused intensity of 4.5 kW/cm^2 with 5.5 pJ energy. The 300-as SXR pulses generated in our lab[39–41,55] have a pulse energy of (2.9 $\pm$ 0.1) pJ and are focused to 80 μm, thus resulting in a peak intensity of 84 kW/cm^2, i.e. one order of magnitude higher than the synchrotron radiation. Nevertheless, such low peak intensities are not expected to result in energy shifts larger than a few meV.

3. **Non-linear excitations**. The probability for non-linear excitations to occur scales with the peak brilliance of the excitation pulse. Also, the longer such pulse, the higher the probability that non-linear affects will occur. Unfortunately, no theory (that we are aware of) currently considers non-linear excitations to describe XAFS measurements.

For the picosecond domain, synchrotron radiation from the TEMPO-A-UHV photoemission beamline at SOLEIL is used to acquire data with 30 ps duration SXR pulses and to compare the results with sub-300-as duration pulses from our own attosecond SXR beamline. In particular, attosecond XAFS (attoXAFS) measurements in graphite and TiS_2[1] are compared with synchrotron radiation XAFS, total

[1] TiS_2 structure and electrical properties are disclosed in Chap. 4.

electron yield (TEY) and energy-resolved Auger, which are called Auger electron spectroscopy (AES) measurements. Carefully contrasting these measurements potentially permits elucidating the decay channels upon core-shell excitation. XAFS, TEY and Auger electron measurements are performed at the carbon K-shell (1s) at 284 eV and the titanium L_2 and L_3 shells ($2p_{1/2}$ and $2p_{3/2}$) at 460 eV and 454 eV. These core-shell electrons are also accessible with the broadband spectrum of the SXR attosecond pulses generated via HHG in the table-top source of our lab.

Considering the typical few femtosecond decay time of Auger processes, our conjecture is that the attosecond SXR pulse probes material's states before such a decay occurs, thus it "sees" the material in its true and unperturbed electronic configuration. Differences in the electronic configuration are attempted to be found on spectral signatures when comparing XAFS measured with 30 ps pulses (TEMPO) with XAFS measured with attosecond-duration pulses (attoXAFS) from our own beamline. These spectral differences are expected to be located at energies close to the absorption edge, as for example absorption edge shifts and changes on the electronic transitions to the conduction band. Moreover, spectral differences between TEY and XAFS measurements are also expected to be found because TEY averages over mirror charge effects and electron scattering within the material whereas XAFS does not.

Note that while XAFS with synchrotron radiation has already been performed in Graphite[130] and TiS_2[108], no accurate Auger analysis exists to elucidate the underlying effects. Here, we conduct additional measurements of XAFS and TEY as a function of angle to provide the electronic contribution of in-plane σ^* states and out-of-plane π^* states, and AES. Using TEMPO synchrotron beamline, XAFS is measured in transmission as a function of the incidence wavelength. To investigate the angular dependence on the XAFS measurements the sample is rotated to address out of plane orbitals. Since the corresponding transition states have been seen to appear at around 30 eV relative to the main absorption edges with a wavelength shift of around 1 eV on glycine[109], an energy resolution of 30 meV is required in both soft-X-ray photon spectrum, TEY and AES. The high energy resolution of 30 meV at 400 eV is obtained in the low energy optical path by using a 1500 t/mm grating that reflects spectral energy from 180 eV to 540 eV. A Scienta SES 2002 electron energy analyser is used for the AES measurements while the TEY measures the current generated through the sample. As for the XAFS measurements the sample is mounted on a silicon photodiode that detects the transmitted photons generating a current that is registered using the TEY detection channel.

Homogeneity of the samples is still important in the synchrotron measurements to ensure that the same composition and thickness is always probed. The

spot size of the beam at the sample plane is of 30 x 80 μm^2 which puts constrains on the sample area and on the maximum angle of incidence to insure that the sample is probed homogeneously across the entire X-ray beam. The TiS_2 and graphite samples are highly ordered single crystals with flat surface and have a homogeneous thickness across at least 100 μm diameter or larger depending on the sample. Each sample rests on a transmission electron microscopy (TEM) grid with a diameter of 3.05 mm made of copper, see Fig. 3.9.

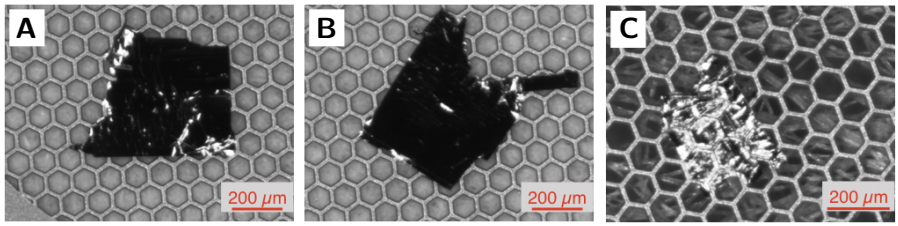

Fig. 3.9: Microscope images of the samples which are measured using synchrotron radiation at SOLEIL. (**A**) 100 nm thick graphite flake used for XAFS. (**B**) 100 nm thick graphite flake used for TEY and AES. (**C**) 150 nm thick TiS_2 flake used for XAFS, TEY and Auger electron spectroscopy. The samples rest on a honey comb TEM grid with mesh 200 (97 μm hole size).

The thin samples, resting on the TEM grids, are transferred on a non-magnetic sample holder made out of thin sheets of Ta that are fixed on a more robust sample holder used to transfer the sample inside the ultra high vacuum (UHV) chambers. Figure 3.10 shows the samples assembly for the different measurements: TEY, Auger electron and XAFS spectroscopy.

For completeness of each measurement, a reference signal is required that takes into account the spectral composition of the incident beam. The reference signals for Auger and TEY measurements are taken with a clean gold surface due to its flat response in the desired energy regime. The gold surface is always sputtered (with Ar^+ ions for 30 minutes) before being measured and kept in a UHV during the whole time in which the measurements are taken. As for XAFS, the reference signal for the photodiode response is taken in transmission through the TEM grid to a position where there is no sample. An X-ray photoelectron spectroscopy (XPS) analysis is taken to ensure the correct sample is being probed and to know its exact composition.

On the following sections the data measured on each sample is presented. Our goals are:

1. to compare TEY with XAFS using the same X-ray source with the same absolute energy calibration - differences on the position peaks are expected due to the work function and electron screening of the material;

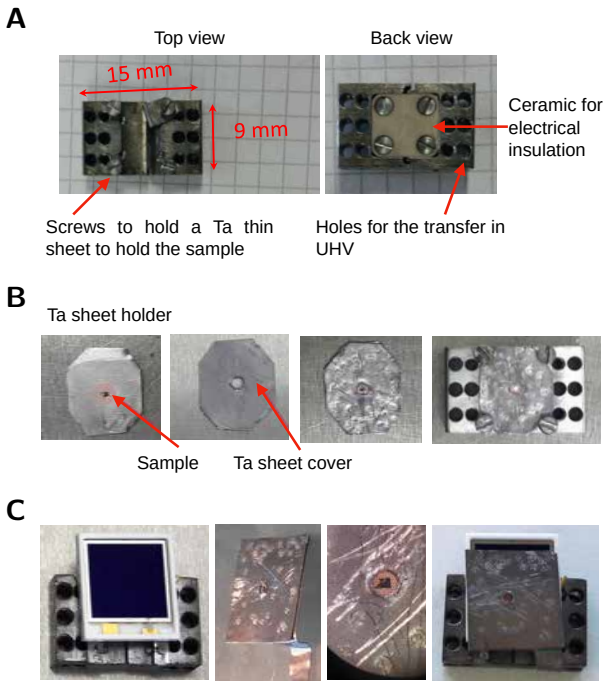

Fig. 3.10: Sample assemblies: (**A**) Robust sample holder used to transfer the sample inside the vacuum chambers. The sample holder is composed by two parts that are held with a ceramic to ensure electrical insulation. One of the parts is connected to an ammeter to measure the current generated through the sample. (**B**) Sample assemblies for TEY and AES measurements. The TEM grid is encapsulated between two welded Ta sheets that are screwed on to the holders shown in (A). (**C**) Sample's assembly for XAFS measurements. A silicon photodiode is put in contact with (A) from which the generated current is measured. A new Ta sheet holder is designed to ensure the detection of the transmitted photons through the sample. This Ta holder is attached to (A) only to one side to ground the sample and prevent the detection of current through the sample.

2. to compare XAFS using synchrotron radiation with XAFS using isolated attosecond pulses (attoXAFS); and

3. to assign an Auger electron analysis to differences found in (2) to possible transition states.

3.3.1 attoXAFS, XAFS, TEY and AES in Graphite

When initiating transmission measurements we found that the graphite samples were too thick to perform XAFS measurements with the photodiode assembly. Only the 1s $\rightarrow \pi^*$ transition at normal incidence angle provided a meaningful

measurement. This transition is expected to absorb less than the 10% of the 1s $\rightarrow \sigma^*$ transition. By increasing the incidence angle both the probed sample thickness and the 1s $\rightarrow \pi^*$ transition are incremented which led to the 1s $\rightarrow \pi^*$ transition becoming saturated. The peak position of the transition 1s $\rightarrow \pi^*$ at normal incidence can still be compared with both the TEY measurements and attoXAFS; see Fig. 3.11. TEY is measured before and after annealing the graphite sample at 200°C (not shown), but no relevant effects are found.

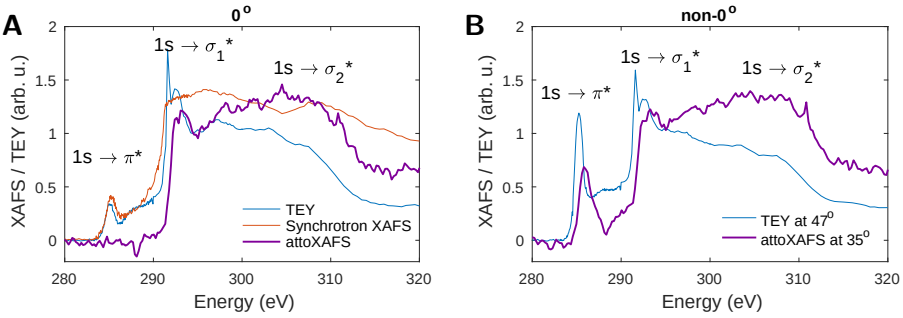

Fig. 3.11: Comparison of synchrotron XAFS, TEY and attoXAFS in graphite. (**A**) At normal incidence angle (0 deg.) the 1s $\rightarrow \sigma^*$ transition is predominant. The synchrotron XAFS saturates above the 1s $\rightarrow \pi^*$ at 285.2 eV. (**B**) By increasing the angle of incidence ($>$ 0 deg.), the 1s $\rightarrow \pi^*$ peak emerges. The energy calibration is kept the original from each measurement.

1s $\rightarrow \pi^*$ transition increases with increasing the angle of incidence for TEY and XAFS using synchrotron radiation or attoXAFS. In TEY and XAFS with synchrotron radiation, the 1s $\rightarrow \pi^*$ transition appears in the spectrum with a width of 1 eV at 285.2 eV. Whereas in attoXAFS this transition is 50% wider (1.5 eV) and appears at a slightly different energy of 285.8 eV. This energy shift is also seen at the absorption edge position of the 1s $\rightarrow \sigma_1^*$ transition position. The most significant spectral differences are found in the 1s $\rightarrow \sigma^*$ transition. 1s $\rightarrow \sigma_1^*$ is stronger than the 1s $\rightarrow \sigma_2^*$ transition in the TEY analysis, but it appears the other way around in attoXAFS. Moreover, the 1s $\rightarrow \sigma_1^*$ transition exhibits a sharp pre-peak that either is not visible or has much smaller contribution in the attoXAFS spectrum.

An Auger electron analysis is performed in two separate measurements, firstly for low binding energies from -7 eV to 45 eV with an energy step of 0.1 eV to analyse the valance electrons and to discriminate from non-desired signals, see Fig. 3.12. Afterwards with a binding energy from -7 eV to 120 eV with an energy step of 0.2 eV to visualise possible Auger electron energy shifts at higher energies which are shown in Fig. 3.13. The kinetic energy, $E_{kinetic}$, is calculated by using $E_{binding} = E_{photon}$ - $E_{kinetic}$, where $E_{binding}$ is the binding energy and E_{photon} is the monochrome incident photon energy.

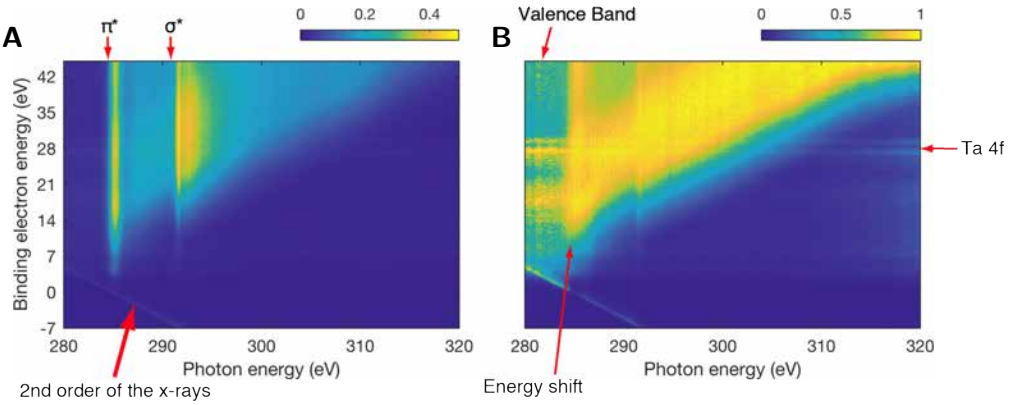

Fig. 3.12: Auger measurement in graphite. (**A**) Binding electron energy as a function of photon energy. (**B**) Normalised signal at each photon energy from (A). Signals with constant binding energy along different photon energies correspond to photon peaks. Auger signals increase linearly in binding energy as a function of photon energy. The different features on the signal are identified as: 1) the π^* and σ^* peaks whose signal strengths decreased by increasing the photon energy; 2) A 2nd order photon peak of the X-rays ionising the 1s state of Carbon; 3) A Ta 4f photon peak that contaminant the signal; and 4) Valence electrons appearing at photon energies lower than the resonant π^* peak. The π^* peak at a photon energy of 285 eV consists of 2 sub-structures, at binding energies of 15 eV and 27 eV, that emerge in 1) at higher photon energies yielding an Auger energy shift.

By analysing in detail the Auger electrons as a function of kinetic energy and at different photon energy positions, we find differences between the Auger electrons from π^* and σ^* states and quantify the Auger energy shift in π^* towards higher photon energies. This is presented in Figs. 3.12 and 3.14. π^* Auger electrons exhibit a dip in intensity only at the resonance photon energy of 285.2 eV and for a kinetic energy of 265 eV. This dip does not come from the Auger electrons from the valence band (also shown in the Figs. 3.12 and 3.13, and 3.14 in blue). Furthermore, this dip is not present in the σ^* Auger electron spectrum.

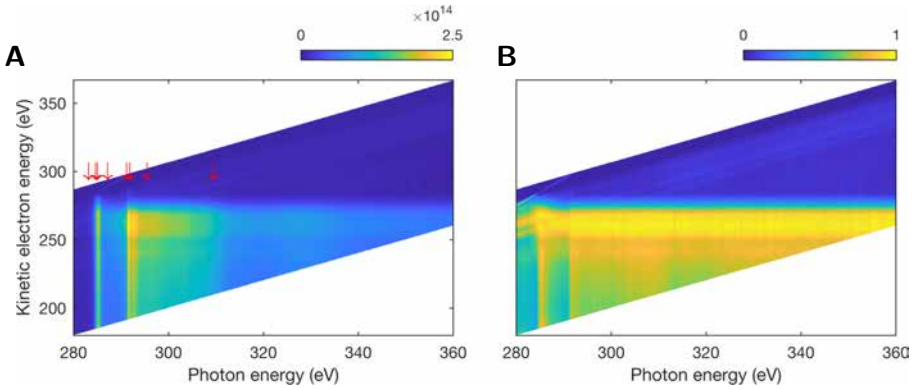

Fig. 3.13: Extended Auger analysis in graphite. (**A**) Kinetic electron energy counts as a function of photon energy. (**B**) Normalised electron counts at each photon energy from (A) as function of photon energy. Signal at a constant kinetic energy along different photon energies corresponds to Auger electrons. Note that there is no Auger electron energy shift at larger photon energies but there is after the π^* peak at 285 eV. Red arrows show the photon energy positions where the Auger electrons' behaviour has been studied in detail.

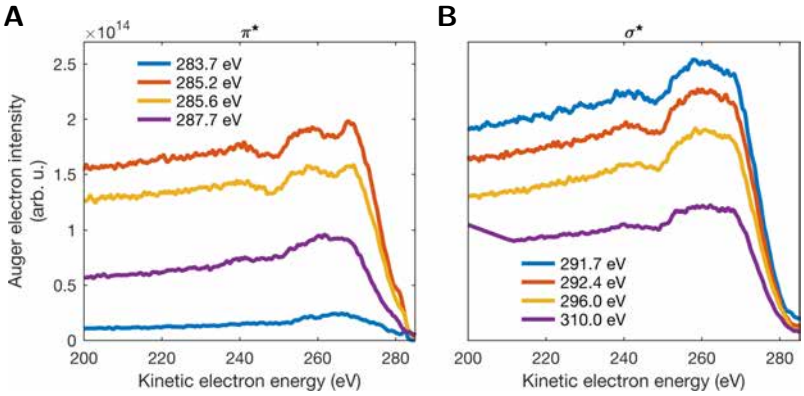

Fig. 3.14: Auger electron intensity as a function of their kinetic energy at given photon energies indicated in Fig. 3.13. (**A**) π^* Auger electrons and (**B**) σ^* Auger electrons at their respective resonant photon energies' vicinities. At a photon energy resonant with π^* Auger electrons at 285.2 eV, a dip is visible with 265 eV electron kinetic energy which is not present for σ^* Auger electrons at resonance.

3.3.2 attoXAFS, XAFS, TEY and AES in TiS_2

A similar analysis to that used with graphite is carried out with TiS_2. XAFS and TEY measured at the titanium L_2 and L_3 edges with synchrotron radiation for different angles of incidence are shown in Fig. 3.15. On both TEY and XAFS (although more prominent in the TEY measurements) a sub-splitting related with the probing of t_{2g} and e_g band manifolds is shown which corresponds to the minimum and the consecutive minimum of the conduction band[2].

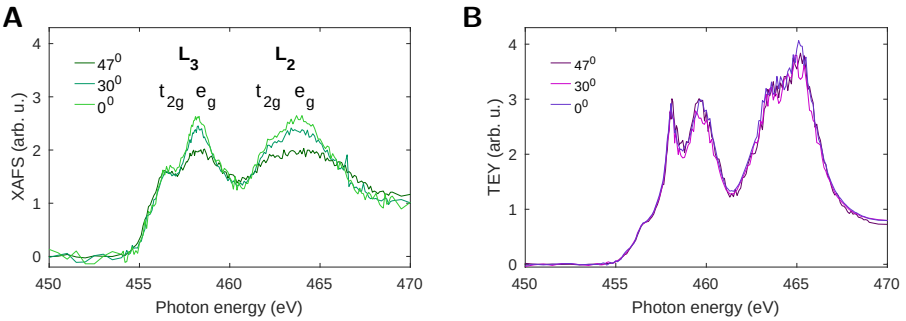

Fig. 3.15: XAFS (A) and TEY (B) in TiS_2 at the titanium L_2 and L_3 edges for different angles of incidence using synchrotron radiation at SOLEIL. L_2 and L_3 appear at a larger energies than the nominal binding energy of monoatomic titanium at 460.2 eV and at 543.8 eV, respectively. Each L transition has a sub-splitting related with the probing of t_{2g} and e_g band manifolds at the minimum, and consecutive minimum, of the conduction band.

Figure 3.16 compares the different techniques, TEY and XAFS, using the same synchrotron source (SOLEIL). Clearly, TEY and XAFS spectra are not identical. The most prominent feature is an energy offset of the TEY by 1 eV towards higher energies. The pre-peak found in the TEY spectrum coincides with the peak at lower energies (t_{2g}) present in XAFS spectrum.

The XAFS measured with the synchrotron radiation is also compared, at normal incidence, with the attoXAFS measurements performed with our own attosecond beamline. Both, attoXAFS and the comparison are shown in Fig. 3.17 and agree well with literature values[108].

The attoXAFS spectra are superimposed with an absorption measurement on an amorphous titanium filter with a thickness of 200 nm which is typically used for the energy calibration of the attosecond beamline. The titanium L-edges of TiS_2 are shifted with respect to the filter reference by 2 eV towards higher energies. The attoXAFS spectrum is shifted by 3 eV towards higher photon energies with respect to XAFS performed in the synchrotron. Both attoXAFS and XAFS in SOLEIL

[2] The TiS_2's band structure is shown in Fig. 4.1 in Chap. 4, Sec. 4.3.1

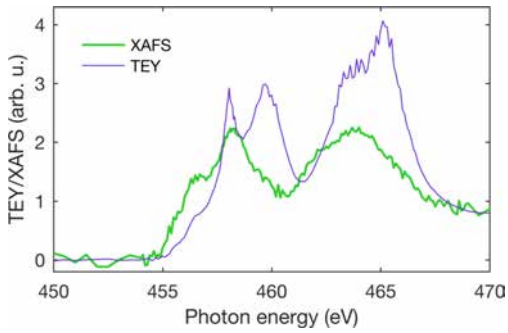

Fig. 3.16: Comparison between XAFS and TEY of TiS_2 at titanium $L_{2,3}$ using the same synchrotron radiation source SOLEIL. The TEY spectrum exhibits a is 1 eV energy shift towards higher energies showing a pre-peak that is positioned at L_3 t_{2g} peak in the XAFS spectrum.

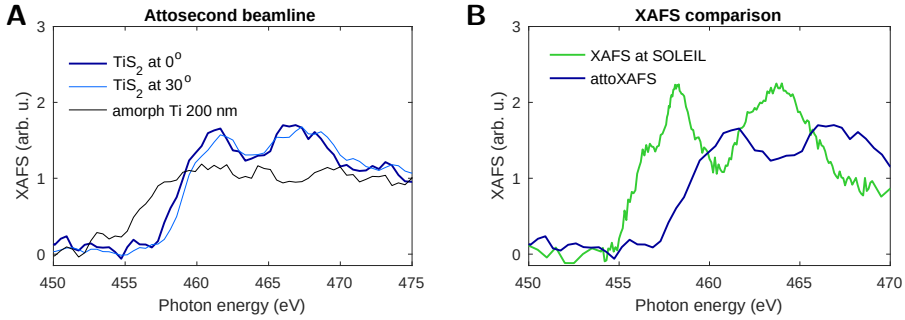

Fig. 3.17: AttoXAFS and XAFS comparison of TiS_2 at titanium $L_{2,3}$. (**A**) AttoXAFS, XAFS measured using attosecond pulses in our beamline. Also shown is the absorption of a 200 nm titanium filter as reference. (**B**) AttoXAFS comparison with XAFS using synchrotron radiation at normal incidence. Although the spectral shape is similar, the attoXAFS spectrum exhibits a 3 eV energy shift towards higher energies in comparison with XAFS using synchrotron radiation.

show a decrease of the L_2 and L_3 transitions as a function of angle. However, TEY does not exhibit significant spectral differences as a function of the angle of incidence. Absorption measurements show a similar height for L_2 and L_3 peaks, whereas, TEY measurements have more subtleties, the counts contribution of L_3 is smaller than the contribution of L_2.

To have a deeper insight into the absorption edge shift between attoXAFS and XAFS, the titanium $L_{2,3}$ edges in both TiS_2 and titanium filter are measured using another synchrotron facility such as PGM beamline of the Physikalisch-Technische Bundesanstalt at BESSY II synchrotron in Berlin (Germany). The results and the source comparison are shown in Fig. 3.18.

Both attoXAFS and XAFS in BESSY II have the titanium L-edges of TiS_2

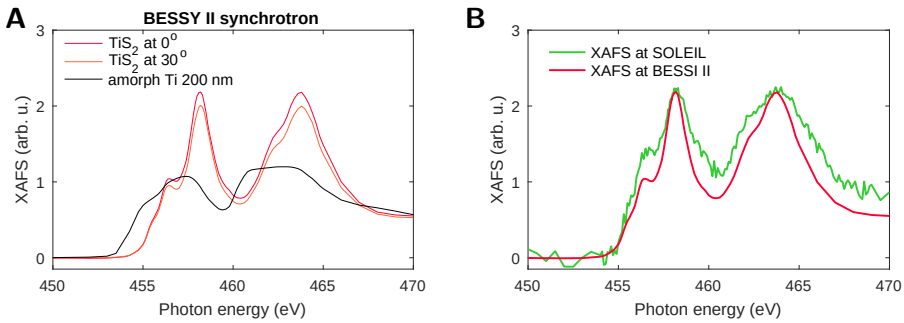

Fig. 3.18: XAFS in BESSY II synchrotron. (**A**) XAFS in the titanium $L_{2,3}$ edges of TiS_2 measured using the synchortron radiation from BESSY II. Overplayed with the absorption of a 200 nm titanium filter. (**B**) Comparison of the XAFS measured in BESSY II with SOLEIL at 0 deg. of incident. The shown data is only normalised to an edge jump = 1.

shifted respect to the filter towards higher energies 2 eV and 1.5 eV, respectively. One could think that the main energy shift of the absorption edges comes from an error in the energy calibration of the beamlines. To refute that, one can overlap both XAFS spectra of the filter absorption edges at the same energy position and there would still be an energy shift of 0.5 eV towards high energies of the attoXAFS spectra respect to the XAFS spectra using synchrotron radiation.

An Auger electron spectrocopy (AES) analysis is performed for binding energies between -10 eV to 175 eV with an energy step of 0.2 eV at an angle of incidence of 47 deg. The sample is not annealed to avoid influencing the TiS_2 composition, hence contaminants might possibly remain on the samples surface. Figure 3.19 shows the Auger electron intensity as a function of their kinetic and exciting photon energy. L_2 and L_3 of titanium with their sub-peaks t_{2g} and e_g are clearly identified at photon energies between 454.7 eV and 465 eV. The long scan at higher energies is performed to ensure the absence of other unexpected features.

The Auger electrons intensity at the resonant photon energies are displaced in Fig. 3.20. The photon peaks contribution, taken at 454.7 eV photon energy, is subtracted to each Auger electron spectrum. Before the subtraction, the photon peaks spectrum is shifted in kinetic energies such that the photon peak positions match.

In both the L_2 and L_3 edges, e_g has a stronger Auger signal than t_{2g} which could be related to e_g manifesting a stronger absorption signal. The lack of literature in Auger emission from TiS_2 force us relate the Auger peaks with the monatomic titanium metallic case[138,139]. In Fig. 3.20(A), the small bump at 332 eV is assigned to the $L_3M_1M_1$ transition. Consecutively there are two bumps

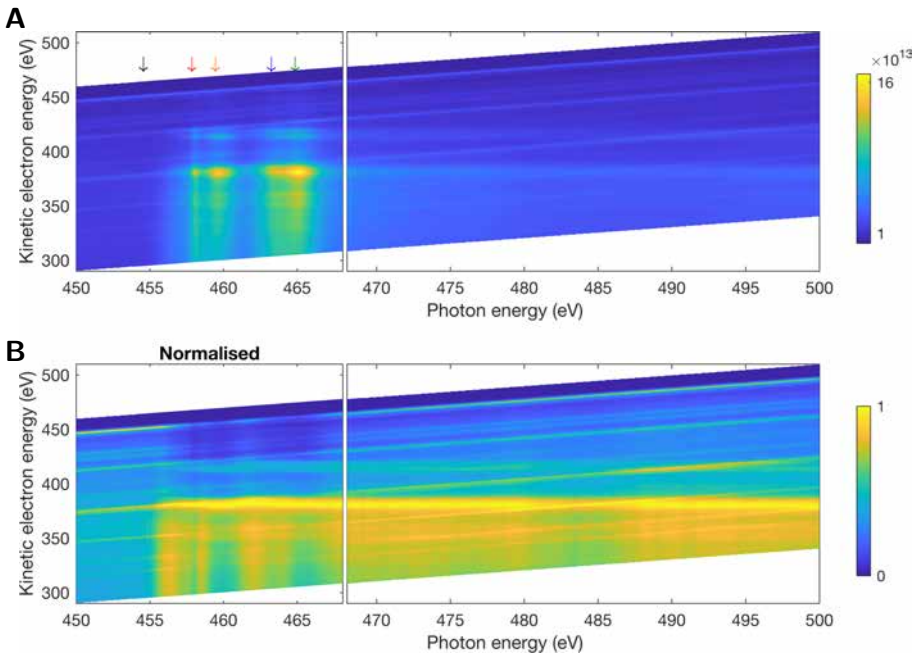

Fig. 3.19: Auger electron spectra at the titanium L_2 and L_3 edges of TiS_2. (**A**) Kinetic energy resolved Auger electron counts as a function of incident photon energy. Displaced arrows show the photon energy position of the valence electrons (black arrow) and resonant Auger electrons from L_3 t_{2g} (red arrow), L_3 e_g (orange arrow), L_2 t_{2g} (blue arrow) and L_2 e_g (green arrow). (**B**) Normalised kinetic energy resolved Auger electron counts from (A) at each photon energy spectra. The Auger electron scan is measured in two separate sets of data due to a loss of beam at the beamline while measuring the first scan at low photon energies.

at 352 eV and 361 eV that correspond to the the $L_3M_1M_{2,3}$ and $L_3M_1M_{2,3}$ transitions, respectively. The main two peaks at 380 eV and 416 eV are related with the transitions $L_3M_{2,3}M_{2,3}$ and $L_3M_{2,3}M_{4,5}$, respectively. The small bump at higher energies at 448 eV it is related to $L_3M_{4,5}M_{4,5}$. The two main peaks have an unidentified post-peak at higher energies around 400 eV and 420 eV that were not present in the monoatomic analysis.

Semi-empirical calculations for Auger decays of Ti[105,140] and Ti^{+4} [141] pointed out that the broadening of the L_2 edge compared to L_3 is due to Coster-Kronig Auger decays. By comparing the width and spectral intensity of the Lorenzian peaks in both L_2 and L_3, the decay time associated with an emission of a Coster-Kronig Auger electron can be extracted[142]. In addition, the post peaks found at 400 eV and 420 eV, at consecutive higher energies of the main $L_3M_{2,3}M_{2,3}$ and $L_3M_{2,3}M_{4,5}$ transitions, respectively, can be assigned to spectator Auger electrons since we are probing at the resonant photon energy. By comparing the peak

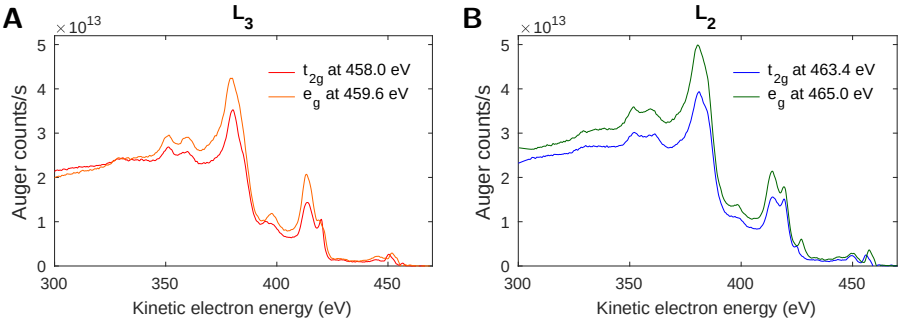

Fig. 3.20: Auger electron counts as a function of their kinetic energy for given resonant photon energies indicated in Fig. 3.19 from the L_3 (A) and L_2 (B) edges. The Auger electron curves are subtracted to the photon peak contribution taken at 454.7 eV (black arrow in Fig. 3.19) which is shifted in kinetic energy to match the photon peak positions. The integration time at each photon energy is 3 seconds with a waiting time of 2 seconds before the measurement starts.

intensity one could also extract life times of the spectator Auger processes[110]. However, to extract the life times of both Coster-Kronig and spectator Auger electrons from the presented current data a more complex theory based in DFT calculations is needed.

Moreover, the L_2 and L_3 edges resonant Auger electrons exhibit different features only at kinetic electron energies between 420 eV, 430 eV and 460 eV. The L_2 edge presents a stronger peak at 420 eV and new peaks appear at 430 eV and at 460 eV. Comparing at the same absorption L-edge in terms of the t_{2g} with e_g contributions, e_g is seen to have a peak at 400 eV in the L_3 edge and at 430 eV in the L_2 that is much stronger than the t_{2g}. Although these differences require of extra theory for an accurate explanation, we suggest their origin is from the different orbital symmetry of the excited photo-electron final state, where t_{2g} has a more d_{z^2} character and e_g is dominated by d_{xy}, although both belong mainly to the titanium atom[143].

3.3.3 Spectral changes of attoXAFS vs. synchrotron XAFS

The first results when comparing XAFS near the absorption edge using synchrotron radiation with an attosecond source is that attoXAFS measurements are shifted towards higher energies by 0.5 - 0.6 eV at 285 eV (0.2% at the carbon K-shell edge) and by 3 eV at 455 eV (0.7% at the titanium L-shell edges) with respect to the XAFS spectra with synchrotron radiation. This could be explained by a change of the energy levels caused by the long synchrotron pulse durations through either electronic and vibrational dynamics or non-linear excitations. These effects may

also be the reason for the different σ transitions in graphite. Such a large energy shift cannot be explained by field effects on the energy levels and remains an unanswered question. It is interesting to point out that the measured EXAFS, using the broadband attosecond SXR pulse, leads to an overestimation (of 6%) in the carbon bond lengths in comparison with values found in literature which were measured using synchrotron radiation sources (see Sec. 3.2.2). This result could be justified by the initialization of vibrational dynamics in the following way: after the photo-excitation of the electron due to the SXR absorption and the consecutive relaxation of the system via an electron decay, vibrational changes in the crystalline structure are induced, this can only be probed by pulses with durations on the order of the vibrational oscillation period. Attosecond pulses can initiate vibrational dynamics but attoXAFS will not be influenced by them. Whereas XAFS using synchrotron radiation will since it has pulse durations on the order of ps on average. The XAFS spectrum over the different bond lengths changes along the vibrational oscillation period, results in an averaged bond length being obtained.

Moreover, the broadening of the 1s $\rightarrow \pi^*$ transition in graphite with a width of 1.5 eV at FWHM when measuring attoXAFS with respect to 1 eV when using synchrotron radiation, could be related to a decrease in the mean free path of the photo-excited electron due to the simultaneous multiple electron excitation.

Another very interesting result, is the fact that although using the same radiation source, the XAFS and TEY are not identical. Interestingly enough, the TEY in TiS_2 exhibits a pre-peak that coincides in energy with the peak at lower energies (t_{2g}) present in the XAFS spectrum. This effect could be explained by charge screening that takes place from the electron excitation until its detection in TEY measurements.

Auger analysis on both graphite and TiS_2 present a different resonant Auger electron spectra depending on the transitions. It will be difficult to link this to the X-ray pulse structure without new theory. The observation could however be explained as having different initial states that lead to different final states due to selection rules. It would also be very interesting to match those spectral differences to inner core dipole transitions to the valence and conduction bands. Hole formation is a direct transition but Auger electrons are secondary transitions, thus more difficult to interpret.

In conclusion, all of the presented results are interesting, partially non expected and support our initial assumptions. Several of these results are under theoretical scrutiny which includes time dependent effects, such as charge migration, dynamics stark shifts, atomic relaxation and structural vibrations.

3.4 Conclusion

In this chapter, the element-specificity characteristics of XAFS due to the electron excitation from a bounded state have been presented. The creation of the dipole transition from an inner core shell to the conduction band follows the selection rules bringing sensitivity to the orbital character of the empty final states thus sensitive to the filling of the final state bands, i.e., it is sensitive to the valence of chemical species. Moreover, due to the dependency on the product $\tilde{d} \cdot \tilde{E}$, XAFS gives sensitivity with respect to anisotropic properties of the electronic structure of a solid. Provided we have an energy-tunable source of X-rays a single absorption edge on certain materials or a variety of edges can be probed simultaneously.

In conclusion, attoXAFS is a powerful new tabletop methodology to simultaneously probe electronic states and atomic positions in condensed phase. AttoXAFS is validated through a simultaneous identification of the σ^* and π^* orbitals in graphite in synchronicity with the material's four characteristic bonding distances[144]. Further, the change of angle of incidence of the attosecond pulse permits distinguishing the various orbital contributions to the density of state of the material. Simultaneous investigation of electronic states and lattice conformation permits the in-situ identification of electron-phonon coupling and to image how multi-body correlations arise during a material's phase transition. This work thus provides a powerful real-time investigative tool that can be used to access the characteristic time-scale of electronic motion to resolve charge migration, electron-nuclear scattering and structural transitions.

Furthermore, the comparison between using an attosecond SXR source and a synchrotron source when performing XAFS spectroscopy shows spectral differences potentially related to induced electron and vibrational dynamics due to the synchrotron long pulse duration. An extended theory is still required to link AES, TEY and XAFS using synchrotron radiation with attoXAFS to decouple the different electron dynamics involved on each of the measurements, respectively. This deep understanding of the dynamic energy states involved in the spectroscopic techniques is essential to distinguish the ground state properties from transition excited states.